ACS APPLIED ELECTRONIC MATERIALS

pubs.acs.org/acsaelm Article

Room Temperature Quantum Anomalous Hall Insulator in a Honeycomb−Kagome Lattice, Ta_2O_3, with Huge Magnetic Anisotropy Energy

Ping Li, Yue Ma, Yun Zhang,* and Zhi-Xin Guo*

Cite This: *ACS Appl. Electron. Mater.* 2021, 3, 1826−1833 Read Online

ACCESS | Metrics & More | Article Recommendations | Supporting Information

ABSTRACT: The quantum anomalous Hall (QAH) effect has attracted enormous attention since it can induce topologically protected conducting edge states in an intrinsic insulating material. For practical quantum applications, the main obstacle is the non-existent room temperature QAH systems, especially with both large topological band gap and robust ferromagnetic order. Here, based on first-principles calculations, we predict the realization of the room temperature QAH effect in a two-dimensional honeycomb−Kagome (HK) lattice, Ta_2O_3, which is a QAH insulator with a non-zero Chern number of $C = -1$. We further found that the non-trivial topological properties are robust against the biaxial strain, where the band gap increases from 80.5 up to 454.8 meV with the strain increasing from 0 to 6%. Moreover, we find that Ta_2O_3 has a huge magnetic anisotropy energy (42.8 meV) and unusual high Curie temperature (788 K). The robust topological and magnetic properties make Ta_2O_3 have great application potentials in room temperature spintronics and nanoelectronics.

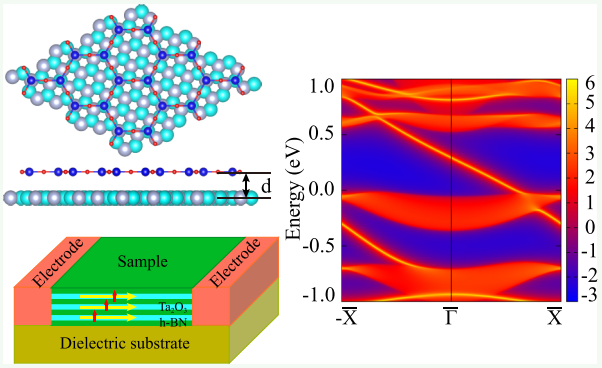

KEYWORDS: *quantum anomalous Hall effect, room temperature, huge magnetic anisotropy energy, topological properties, first-principles calculations*

Downloaded via XI'AN JIAOTONG UNIV on April 27, 2021 at 08:23:45 (UTC).
See https://pubs.acs.org/sharingguidelines for options on how to legitimately share published articles.

INTRODUCTION

Topological materials have attracted extensive attention because of their intriguing transport properties.[1−4] Especially, the quantum anomalous Hall (QAH) insulator, also called as the Chern insulator, is a two-dimensional (2D) magnetic insulator with the non-zero Chern number and quantized Hall conductivity in the absence of an external magnetic field as put forward first by Haldane in his Nobel Prize-winning paper.[5] The quantized conductivity is written as $\sigma_{xy} = C(e^2/h)$; the Chern number (C) is equal to the number of gapless chiral edge states along an edge of the finite width nanoribbon. These chiral edge states are robust against any impurity perturbations and topologically protected. Because of the novel non-trivial topological characteristics and desirable potential applications for designing low-energy spintronics and electronics, extensive theoretical research has recently been carried out to find real QAH insulators.[6−23]

So far, the QAH effect has been experimentally reported in V/Cr-doped $(Bi,Sb)_2Te_3$ films at an extremely low temperature and the van der Waals-layered material $MnBi_2Te_4$ at 1.4 K.[24−27] For practical applications, it is of significance to search for QAH insulator materials with a huge magnetic anisotropy energy (MAE), large band gap, high carrier mobility, and simultaneously high Curie temperature (T_c).[4] On the other hand, the low carrier mobility may be caused by the disorder on account of the doped magnetic atoms, whereas the weak magnetic coupling may be derived from the localized V/Cr-3d orbitals that scarcely overlap with the orbitals of the adjacent V/Cr atoms. The problems of the small band gap and weak magnetic coupling could be overcome by importing 5d transition metal atoms that synchronously have more expanded d orbitals and stronger spin orbital coupling (SOC). Obviously, it would be meaningful to look for the high T_c QAH effect in ferromagnetic (FM) 5d transition metal materials.

In this paper, we predict that a 2D honeycomb−Kagome (HK) lattice, Ta_2O_3, is a room temperature Chern insulator with large MAE, which is characterized by non-zero Chern number −1 and chiral edge states. Moreover, the spin-polarized band structure indicates that the biaxial strain could drive metal to half-metal transitions. More interestingly, it shows that the Dirac

Received: January 25, 2021
Accepted: March 26, 2021
Published: April 6, 2021

ACS Publications © 2021 American Chemical Society

half-metals are characterized with a Curie temperature of T_c = 451 K at the 6% strain. It is worth noting that the non-trivial topology property is robust under in-plane biaxial strain, and its band gap can be up to E_g = 454.8 meV, which is far larger than the lately predicted E_g = 10 meV in the manganese halide MnI_3.[19] Finally, we find that h-BN is the ideal substrate for its synthesis and device fabrications. These findings on the Ta_2O_3 system open a way to the investigation of the room temperature QAH effect.

STRUCTURES AND COMPUTATIONAL METHODS

To explore the magnetic and electronic structures, we used Vienna *Ab initio* Simulation Package (VASP)[28,29] for the first-principles calculations based on density functional theory (DFT) and applied the generalized gradient approximation (GGA) of the Perdew−Burke−Ernzerhof functional as the exchange−correlation potential.[30] The plane-wave basis set with a kinetic energy cutoff of 500 eV is applied. Here, 12 × 12 × 1 and 24 × 24 × 1 Γ-centered *k* meshes are employed for the structural relaxation and the self-consistent calculations, respectively. The energy convergence criterion is set to be 10^{-6} eV. To affirm the structural stability, the phonon spectra are calculated using a finite displacement approach as used in the PHONOPY code.[31] Thermal stability is confirmed with a 4 × 4 supercell at 300 K using first-principles molecule dynamics (MD). Therefore, in order to describe the strongly correlated 5d orbitals of the Ta atom, the GGA + *U* method is employed.[32] Here, we applied linear response theory to evaluate the *U* parameter.[33] The *U* value can be calculated by the response function

$$\chi_{IJ} = \frac{\partial^2 E}{\partial\alpha_I \partial\alpha_J} = \frac{\partial n_I}{\partial\alpha_J} \quad (1)$$

In linear response theory, χ_{IJ} can be acquired from the response of d electron occupations to a small perturbation potential shift α. The effective interaction value *U* related to site I can be rewritten as

$$U = \chi^{-1} - \chi_0^{-1} = \left(\frac{\partial N_I^{SCF}}{\partial V_I}\right)^{-1} - \left(\frac{\partial N_I^{NSCF}}{\partial V_I}\right)^{-1} \quad (2)$$

where χ^{-1} and χ_0^{-1} denote the non-interacting and Kohn−Sham density response functions of the material with regard to the localized perturbation, respectively. Then, the calculated *U* value, based on linear response theory, is 1.79 eV for Ta, as illustrated in Figure S6. In addition, we have used effective *U* values to test calculations, ranging from 0 to 2.6 eV. We employed an effective *U* value of 2 eV for the Ta-5d orbital in our calculations because its result is more reasonable. Moreover, the screened exchange hybrid density functional by HeydScuseria-Ernzerhof (HSE06) is used to test the band structure. To calculate the edge states, we projected the Bloch wave function into maximally localized Wannier functions (MLWFs)[34−36] that originated from the Ta-d and O-p orbitals and made use of the WANNIER-TOOLS package.[37] Therefore, the edge states are calculated under half-infinite boundary conditions using Green's function mean.[36]

RESULTS AND DISCUSSION

Structure and Stability. The geometric structure of the Ta_2O_3 monolayer forms a 2D honeycomb−Kagome lattice with the D_{6h} point group, as illustrated in Figure 1a. The two Ta and three O atoms comprise a (1 × 1) unit cell, featured by sharing one O atom bridged with each adjacent, which is semblable to that of Hg_3As_2 and C_3Ca_2.[38,39] The optimized lattice parameters are $a = b$ = 6.58 Å, and the d_{Ta-O} bond distance is 1.90 Å. The distance of two nearest neighboring Ta is 3.80 Å.

In contrast to the Kagome lattice[40−44] where two metal atoms are bonded by non-metal atoms, two Ta atoms of the Ta_2O_3 monolayer are bonded through two anions (as shown in Figure 1a), which could give rise to fascinating magnetic properties different than the conditions in the Kagome lattice. To evaluate

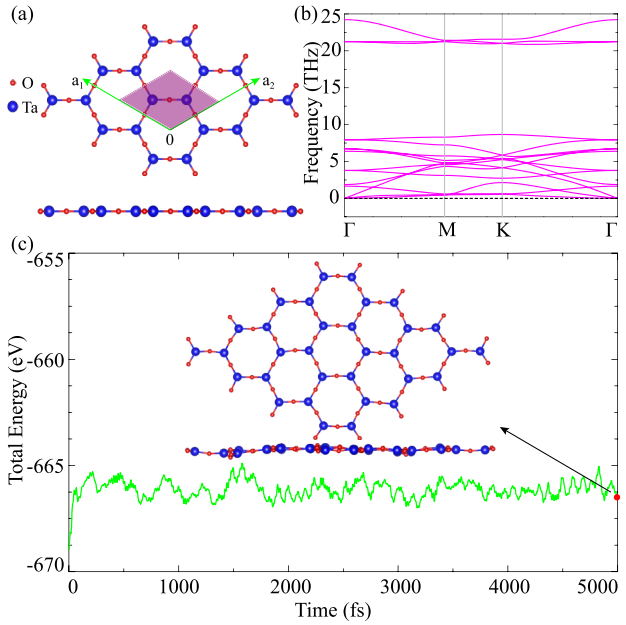

Figure 1. (a) Top and side views of the Ta_2O_3 monolayer with the lattice a_1 and a_2; the unit cell is marked by the purple shading. The Ta and O atoms are denoted by the blue and red balls, respectively. (b) Calculated phonon spectra. (c) Total energy fluctuations of the Ta_2O_3 monolayer during 5 ps MD simulation at 300 K. The final structures after MD simulation are shown in the insets.

the stability of the Ta_2O_3 monolayer, we first calculate the formation energy, $E_f = (E_{Ta_2O_3} - 2\mu_{Ta} - 3/2\mu_{O_2})$, where $E_{Ta_2O_3}$ is the total energy of the Ta_2O_3, while μ_{Ta} and μ_{O_2} are the chemical potential of separated tantalum and oxygen gas, respectively. The formation energy of the monolayer Ta_2O_3 is −5.58 eV/atom. The negative value represents that it is an exothermic process. To check whether the Ta_2O_3 becomes buckled, we consider the buckled Ta_2O_3 lattice. Figure S1 shows the energy differences between different buckled and planar structures. The energies of Ta_2O_3 increase monotonically with the buckled height from 0 to 2.0 Å, which suggests that the stable structure is planar rather than buckled.

To further verify the structural stability of the Ta_2O_3 monolayer, we calculated the phonon spectra, as illustrated in Figure 1b. The lack of a negative value affirms the dynamical stability of the Ta_2O_3. Moreover, we employ molecular dynamics simulations to verify room temperature (300 K) thermal stability of Ta_2O_3. As shown in Figure 1c, the lattice structure after annealing at 300 K for 5 ps displays that the Ta_2O_3 almost keeps the original structure unbroken. In the simulation process, the small fluctuations of energy with time further affirm its thermal stability.

Magnetic Properties. To explore the preferable magnetic properties of Ta_2O_3, we first consider two probable magnetic configurations, in other words, FM and antiferromagnetic (AFM) states to confirm the ground state. The FM configuration is found to be 832.93 meV lower in energy than the AFM configuration per unit cell, definitely denoting that the FM phase is the ground state of Ta_2O_3. The magnetic moment is 4 μ_B per unit cell, which is consistent with the Bader charge analysis. The spin configuration is $d^{2\uparrow 0\downarrow}$ of Ta^{3+}.[45] The easy axis anisotropy is significant to the existence of the QAH effect in Ta_2O_3 because the band gap retains zero in the spinor along the *x* axis. Moreover, we calculated the magnetic anisotropy energy

https://doi.org/10.1021/acsaelm.1c00085
ACS Appl. Electron. Mater. 2021, 3, 1826−1833

(MAE) reaching up to 42.8 meV and found that the easy axis is vertical to the in-plane. We also calculate shape anisotropy contribution to the MAE due to its completely planar structure. For FM ordering, the shape anisotropy E_S of a perfectly flat film is given as

$$E_S = -\frac{1}{2}\frac{\mu_0}{4\pi}\sum_{i=1,N}\sum_{j=1,\max}\left[\frac{\vec{m}_1\cdot\vec{m}_2}{r_{ij}^{\ 3}} - \frac{3}{r_{ij}^{\ 5}}(\vec{m}_1\cdot\vec{r}_{ij})(\vec{m}_2\cdot\vec{r}_{ij})\right] \quad (3)$$

where the negative sign indicates that an in-plane easy axis is favored. We take 2 μ_B for m and atomic volume of the Ta atom. In our calculations, we find values of $E_S = -0.037$ meV per unit cell for Ta_2O_3, which are much smaller than the MAE.

The Curie temperature is a significant property for experimentally observing the QAH effect at a high temperature. Hence, it is a requirement to comprehend the change in the magnetism with temperature. For the purpose, we use Monte Carlo (MC) simulations on account of the Heisenberg model; the T_c of Ta_2O_3 can be evaluated through applying MC simulations

$$H = -\sum_{i,j} J_{i,j} M_i \cdot M_j - \sum_i A(S_i^z)^2 \quad (4)$$

where $J_{i,j}$ is the nearest-neighbor exchange value, M is the local magnetic moment of the Ta atom, S_i^z is the spin constituted along the z axis, and A is the MAE value. Based on the calculated total energies of different magnetic configurations, J can be obtained by $J = \Delta E/6S^2$, where ΔE is the energy difference between AFM and FM states, calculating the exchange interaction value of 138.82 meV. With the spin Hamiltonian, we employed a parallel-tempering MC simulation on a 100 × 100 supercell to estimate the T_c of Ta_2O_3 to be 788 K, much higher than that of the existing 2D FM materials, as shown in Figure 2b. Therefore, the 2D Ta_2O_3 monolayer is room temperature ferromagnetic.

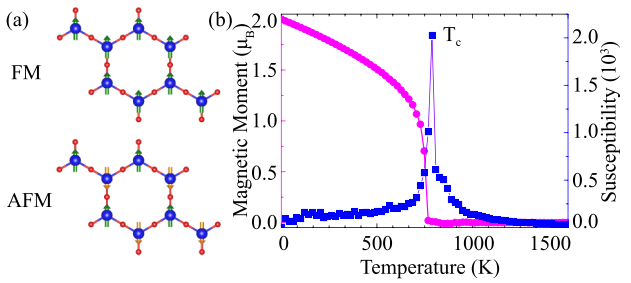

Figure 2. (a) Schematics of different magnetic configurations: FM and AFM. (b) MC simulations, the average magnetic moment (magenta) and susceptibility (blue) per unit cell in regard to the temperature calculated for Ta_2O_3.

Onsite Correlation Tunable Magnetic Properties. To explore the ferromagnetism origin of Ta_2O_3, we calculated the density of states (DOS) of the FM ground state from GGA + U, as shown in Figure 3a. It can be observed that the state near the Fermi level is primarily contributed by Ta 5d electrons. In the 2D Ta_2O_3 lattice, the extremely strong ferromagnetic coupling originates mainly from half-filled spin up d_{yz} and d_{xz}, as shown in Figure 3b. Because spin-up d_{yz} and d_{xz} orbitals of Ta atoms undergo strong orbital hybridization through the bridged oxygen atoms, the double-degenerate d_{yz} and d_{xz} states would be divided into the high-lying anti-bonding states and low-lying

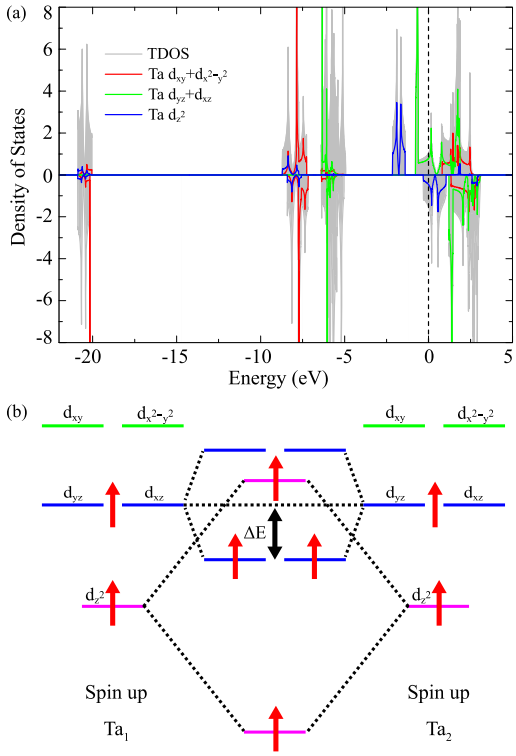

Figure 3. (a) DOS and PDOS of Ta_2O_3 were calculated at the GGA + U level. Obviously, the bands near the Fermi level are mainly by d_{yz} and d_{xz} orbitals. (b) Plot of the magnetic exchange mechanism for the ferromagnetic state. Obviously, the occupation of the low-lying bonding state reduces the total energy.

bonding. The double-degenerate bonding states will be occupied by d_{yz} and d_{xz} electrons. Because E(FM) is in direct proportion to t, while t is the hopping parameter between adjacent Ta atoms, it leads to a decrease in energy. However, when the spins of the two Ta atoms are anti-parallel to each other, the E(AFM) [E(AFM) ∞ t^2/U] will reduce due to the superexchange mechanism. We observe that the energy difference between the FM and AFM states increases, while Hubbard U increases, as shown in Figure 4a. The FM state is independent of U, while the AFM state decreases with U. Evidently, the origin of ferromagnetism is because of direct exchange between Ta atoms.

We further contain SOC in the GGA + U calculation to verify U dependence of the MAE of Ta_2O_3. As shown in Figure 4b, it proves that Ta_2O_3 has a strong easy axis MAE with the spins along the z axis. The FM phase with the spins along the z axis has a lower energy by 3.38 meV/f.u. than that with the spins along the x axis. The MAE increases, while the onsite correlation becomes larger with the orbital moment enlargers, as illustrated in Figure 4c. The easy axis MAE can be comprehended according to degenerate perturbation theory. Since $\langle d_{yz}|\hat{L}_z|d_{xz}\rangle = -i$, while $\langle d_{yz}|\hat{L}_+|d_{xz}\rangle = \langle d_{yz}|\hat{L}_-|d_{xz}\rangle = 0$, the spin conserving term of the SOC operator $\hat{S}_n(\hat{L}_z\cos\theta + 1/2\hat{L}_+e^{-i\phi}\sin\theta + 1/2\hat{L}_-e^{i\phi}\sin\theta)$, where ϕ and θ are, respectively, the azimuth and zenith angles of the magnetization in the direction $n(\theta, \phi)$ could have reduced energy, while all the spins are along the out-plane direction.[46]

More meaningfully, we observe that the band gap of 2D Ta_2O_3 is related to the onsite correlation; as illustrated in Figure 4d, a larger Hubbard U value results in a larger band gap. On account of the poor screening of the Coulomb interactions in the

https://doi.org/10.1021/acsaelm.1c00085
ACS Appl. Electron. Mater. 2021, 3, 1826−1833

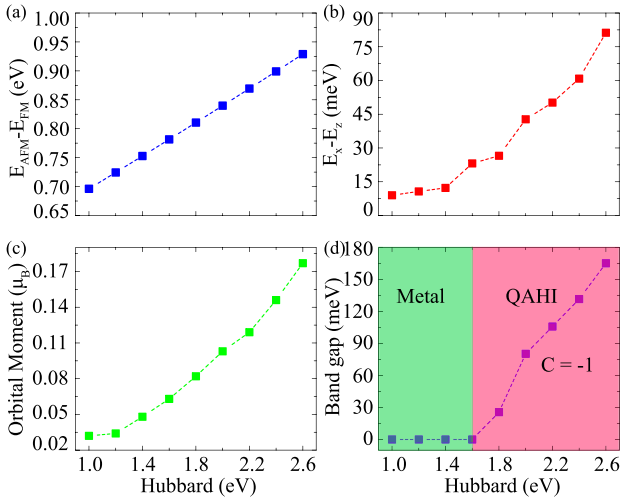

Figure 4. Dependence of physical properties onsite correlation. (a) Energy difference (eV/f.u.) between AFM and FM states. (b) Energy difference the FM state between spinor along the x direction and z direction, meaning that Ta_2O_3 has an easy-magnetization direction along the z axis. (c) Orbital moments of the Ta^{3+} ion. (d) Global band gap. The metal phase persists up to U_c; above U_c lies the quantum anomalous Hall insulator (QAHI) phase.

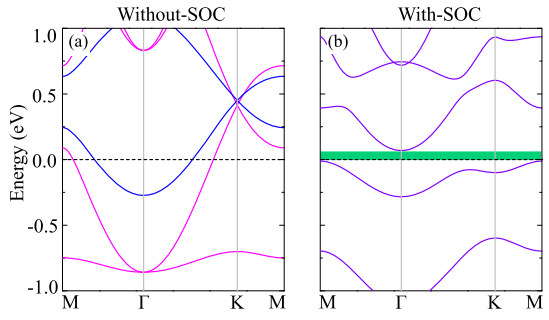

Figure 5. Band structures of the without-strain Ta_2O_3 monolayer. (a) Spin-polarized band structure, the magenta and blue curves correspond to the spin-up and spin-down bands, respectively. (b) Band structures with SOC.

2D monolayer, it is anticipated that the Hubbard U in Ta_2O_3 will be larger than 2 eV. Hence, its actual band gap should be greater than 80.5 meV. The results are further confirmed by the HSE06 method.

Strain-Tunable Electronic Properties. Let us now discuss the main characteristics of the band structure of Ta_2O_3. In the absence of strain, Ta_2O_3 is metallic without SOC, as shown in Figure 5a. A unique set of two bands appears for each spin channel, while intersecting at the K point and forming two Dirac points above the Fermi level. When the SOC is considered, the Dirac cone becomes gapped, as illustrated in Figure 5b. Moreover, the small strain can significantly influence the electronic properties and is thus a useful parameter for tuning system properties. Hence, we implement systematic calculations for the 2D Ta_2O_3 monolayer under different in-plane strains. The FM-phase energy is lower than that of the AFM state under strain, indicating that the FM phase is the ground state, as illustrated in Figure 6a, Generally speaking, although a strong SOC is required to open a sizable E_g, investigations of candidate Chern insulators always assume that their magnetization is vertical to the plane of the two-dimensional system,[47] thus

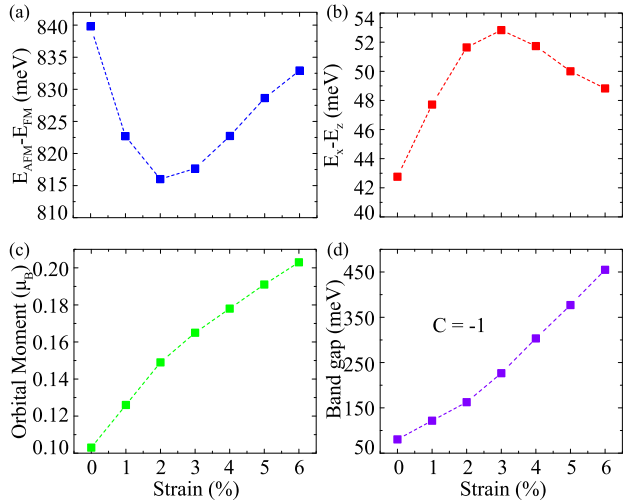

Figure 6. Dependence of physical properties on the biaxial in-plane strain with U = 2.0 eV for Ta. (a) Energy difference (eV/f.u.) with AFM and FM states. (b) Energy difference with the FM state between spins along the x axis and that with spins along the z axis, meaning that Ta_2O_3 has an easy-magnetization axis along z. (c) Orbital moments of the Ta^{3+} ion. (d) Global band gap.

ignoring SOC-generated MAE. The MAE is a basic property of any magnet that chooses an energetically beneficial magnetization direction. The strain can remarkably tune MAE by strong SOC, as shown in Figure 6b. It indicates that a strong easy axis tends to be along the z axis under different in-plane strains. Meanwhile, the MAE changes when the strains become larger; it leads to a larger orbital moment, as illustrated in Figure 6c.

In Figure S2, we show the band structures near the Fermi energy of the strain FM Ta_2O_3. More interestingly, under the strain, the spin-up bands move downward with the strain increasing; meanwhile, the spin-down bands are gradually shifted upward (see the left pannel in Figure S2). Furthermore, the Dirac cone near E_F in the majority spin band structure can be viewed at the 6% strain, which is called as Dirac half-metals with 100% spin polarization, as shown in Figures 7a and S3. Hence, they have the potential to be used in polarization spintronics and optics. In addition, the previously reported Dirac materials, for example, IV-based 2D honeycomb lattices, are featured by the Dirac state originating from the weaker SOC p-orbital.[48−51] As illustrated in Figure 3a, we found that the Dirac states are primarily contributed from Ta-d orbitals.

When including the SOC interaction, these Dirac cones become gapped, as illustrated in the right panel in Figures S2 and 7b. Figure 6d shows the evolution of the global band gap E_g as a function of strain. Obviously, the global gap E_g increases with the strain and reaches up to 454.8 meV at the strain of 6%. To overcome the underestimation of the band gap E_g, we further implement HSE06 to calculate the band structures; see Figure S4. These results are consistent with GGA + U. Considering the influence of the lattice parameter, the suited semiconductor materials, such as SiC, h-BN, MoS_2, and so on, can be applied as substrates to prepare quantum devices in spintronics.

Topological Properties. To affirm the topological properties of Ta_2O_3, we have calculated the local density of states of the edge state through constructing Green's functions[52] for the semi-infinite boundary based on the maximally localized Wannier function method.[34,53] Apparently, the results are illustrated in Figure 7c, in which a single topologically protected

https://doi.org/10.1021/acsaelm.1c00085
ACS Appl. Electron. Mater. 2021, 3, 1826−1833

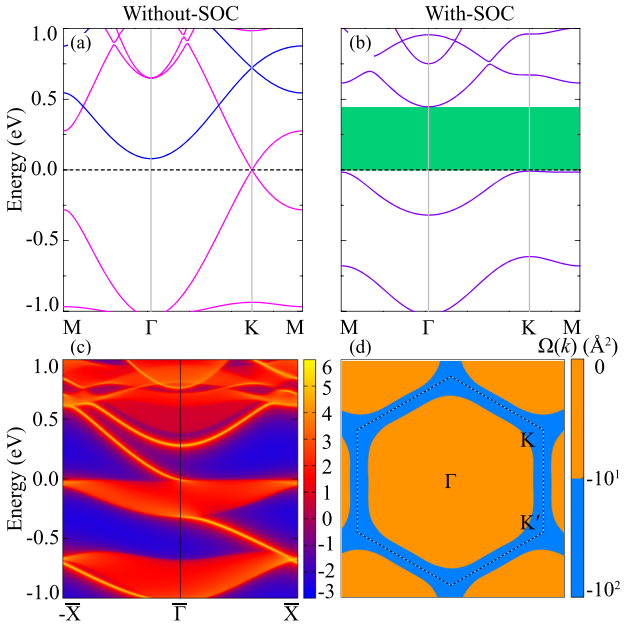

Figure 7. Band structures and topological properties of 6% strain Ta_2O_3. (a) Spin polarized band structure, the magenta and blue curves represent the spin-up and spin-down bands, respectively. (b) Band structures with SOC. (c) Calculated edge state of a semi-infinite sheet of Ta_2O_3. (d) Berry curvature with SOC in the momentum space.

chiral edge state appears in between the conduction band and valence band.

Moreover, the Chern number is calculated from

$$C = \frac{1}{2\pi}\int_{BZ} d^2k\Omega(\boldsymbol{k}) \tag{5}$$

where the Brillouin zone (BZ) stands for the integral over BZ. $\Omega(\boldsymbol{k})$ is the Berry curvature of all occupied bands given as

$$\Omega(\boldsymbol{k}) = -\sum_n f_n \sum_{n'\neq n} \frac{2\mathrm{Im}\langle\psi_{nk}|v_x|\psi_{n'k}\rangle\langle\psi_{n'k}|v_y|\psi_{nk}\rangle}{(E_{n'} - E_n)^2} \tag{6}$$

where v_x and v_y are operator constituents along the x and y axis, respectively, and f_n = 1 for the occupied band.[54] The Berry curvature distribution for the QAH state is shown in Figure 7d. The distribution indicates that the Berry curvature is from the high-symmetry line $K-K'$ with the same symbol. The absolute value of the Chern number is equal to the number of gapless chiral edge states along an edge of the Ta_2O_3 sheet. Our results indicate that the Chern number of the system is −1; this is consistent with the calculated edge state. We found that the non-trivial topological state retains within the strain range of 6%. Surprisingly, the non-trivial band gap is 454.8 meV, greater than the room temperature energy scale ($k_BT \approx 27$ meV at T = 300 K), so we predict that Ta_2O_3 provides a prospective platform for investigating the QAH effect at 451 K, which is 5 orders of magnitude higher than 30 mK temperature of the QAH effect recently observed in a Cr-doped Bi_2Se_3 system.[24]

Tight-Binding Model of the Ta_2O_3 Monolayer. To further understand the origin of the QAH effect, we establish a tight-binding (TB) model for Ta_2O_3. In the 2D Ta_2O_3 system, the topological state is mainly from the Dirac cone near the Fermi level in the spin-up band structure. Hence, we have calculated the real-space distribution of the wave functions in the Dirac cone, as illustrated in Figure S5. It can be distinctly seen that the topological state has the nature of d_{yz} and d_{xz} orbitals of Ta. Therefore, the TB Hamiltonian constructed on the basis of $(d_{A,xz}, d_{A,yz}, d_{B,xz}, d_{B,yz})^T$ can be written as $H = H_0 + H_{SOC}$. H_0 is the nearest neighbor hopping term given as

$$H_0 = t\sum_{i,j} (d^{\dagger}_{j,\vec{R}_i} d_{j,\vec{R}_i+\vec{e}_j} + H.\,c.\,) \tag{7}$$

where $\vec{e}_{1,2} = \pm\frac{\sqrt{3}}{2}\vec{e}_x + \frac{1}{2}\vec{e}_y$ and $\vec{e}_3 = -\vec{e}_y$ are unit vectors from the A site to its neighboring B site. The SOC Hamiltonian is expressed as

$$H_{SOC} = i\lambda\sum_i [(d^{\dagger}_{xz,\vec{R}_i^{(A)}} d_{yz,\vec{R}_i^{(A)}} - d^{\dagger}_{yz,\vec{R}_i^{(A)}} d_{xz,\vec{R}_i^{(A)}}) + +(d^{\dagger}_{xz,\vec{R}_i^{(B)}} d_{yz,\vec{R}_i^{(B)}} - d^{\dagger}_{yz,\vec{R}_i^{(B)}} d_{xz,\vec{R}_i^{(B)}})] \tag{8}$$

in which λ represents the strength of SOC. Finally, the effective Hamiltonian can be given as

$$H(\vec{k}) = \begin{pmatrix} -\lambda + \frac{\varepsilon_{Axz}+\varepsilon_{Ayz}}{2} & \frac{\varepsilon_{Axz}-\varepsilon_{Ayz}}{2} & \frac{t}{2}u(\vec{k}) & \frac{t}{2}v(\vec{k}) \\ \frac{\varepsilon_{Axz}-\varepsilon_{Ayz}}{2} & \lambda + \frac{\varepsilon_{Axz}+\varepsilon_{Ayz}}{2} & \frac{t}{2}w(\vec{k}) & \frac{t}{2}u(\vec{k}) \\ \frac{t}{2}u^*(\vec{k}) & \frac{t}{2}w^*(\vec{k}) & -\lambda + \frac{\varepsilon_{Bxz}+\varepsilon_{Byz}}{2} & \frac{\varepsilon_{Bxz}-\varepsilon_{Byz}}{2} \\ \frac{t}{2}v^*(\vec{k}) & \frac{t}{2}u^*(\vec{k}) & \frac{\varepsilon_{Bxz}-\varepsilon_{Byz}}{2} & \lambda + \frac{\varepsilon_{Bxz}+\varepsilon_{Byz}}{2} \end{pmatrix} \tag{9}$$

where

$$u = e^{i\vec{k}\cdot\vec{e}_1} + e^{i\vec{k}\cdot\vec{e}_2} + e^{i\vec{k}\cdot\vec{e}_3} \tag{10}$$

$$v = \frac{1-i\sqrt{3}}{2}e^{i\vec{k}\cdot\vec{e}_1} + \frac{1+i\sqrt{3}}{2}e^{i\vec{k}\cdot\vec{e}_2} - e^{i\vec{k}\cdot\vec{e}_3} \tag{11}$$

$$w = \frac{1+i\sqrt{3}}{2}e^{i\vec{k}\cdot\vec{e}_1} + \frac{1-i\sqrt{3}}{2}e^{i\vec{k}\cdot\vec{e}_2} - e^{i\vec{k}\cdot\vec{e}_3} \tag{12}$$

Based on this Hamiltonian, we calculate energy bands without and with SOC, as illustrated in Figure 8. The linear Dirac band dispersion is clearly observed, as shown in Figure 8a. When the SOC is included, the Ta_2O_3 is found to be semiconducting with a gap of 700 meV opened at the high-symmetry K points, as illustrated in Figure 8b. These are in a good agreement with DFT

https://doi.org/10.1021/acsaelm.1c00085
ACS Appl. Electron. Mater. 2021, 3, 1826−1833

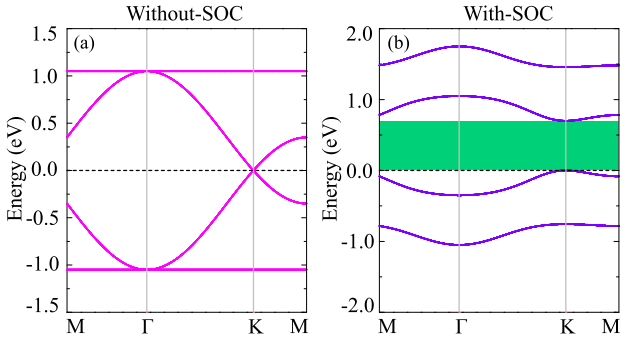

Figure 8. Band structures of 6% strain Ta_2O_3 calculated using the TB model (a) without SOC and (b) with SOC. The parameters are set as t = 0.7 eV for transfer energy and λ = 0.35 eV for the intrinsic SOC.

results. It reveals that the Dirac bands of Ta_2O_3 originated from Ta-d_{xz} and d_{yz} orbitals, which is of significance to realize the QAH effect.

Discussion of the Experimental Synthesis and Potential Application of Ta_2O_3. Recently, Addou *et al.* reported that the Y_2O_3 lattice has been successfully synthesized on platinum-supported graphene.[55] The interaction between graphene and Y_2O_3 is weak, but it is stable at high temperature. Scanning tunneling microscopy displays that the Y_2O_3 shows a two-dimensional hexagonal structure rotated by 30° compared with the graphene. Obviously, the result provides robust evidence to support our predictions. In order to exhibit the practical application in 2D spintronic devices, we investigate the probability of forming a heterojunction on the h-BN substrate. The geometrical structure of 1 × 1 Ta_2O_3 on the $\sqrt{7} \times \sqrt{7}$ h-BN substrate is shown in Figure 9a. The lattice mismatch is defined as $|a_{BN} - a_{Ta_2O_3}|/a_{BN}$, where a_{BN} and $a_{Ta_2O_3}$ are the lattice parameters of the h-BN substrate and Ta_2O_3, respectively. The lattice mismatch ratio is 0.3%. Moreover, we consider van der Waals (optB86b-vdW) corrections in the calculations. After full geometry optimizations, the layer distance of Ta_2O_3 and h-BN is 3.30 Å, displaying a weaker van der Waals interaction. Figure 9b exhibits the calculated energy band of the heterojunction. Without SOC, the Dirac cone still appears at high-symmetry K points. The band gap of 540.6 meV is induced when considering the SOC effect. Considering the wide band gap of the h-BN electrically insulate neighboring QAH layer of Ta_2O_3, the Ta_2O_3/h-BN heterojunction can parametrically increase the number of edge transport channels to sustain the low-power consumption transport, as illustrated in the quantum device constructed with a Ta_2O_3/h-BN heterostructure in Figure 9c. In order to verify that the vdw substrate does not affect its topology, we calculate the Berry curvature, Chern number, and edge state. The non-zero Chern number of $C = -1$ is acquired. In addition, we find that one chiral edge state appears in the bulk band gap, as illustrated in Figure 9d. It is consistent with the Chern number of −1.

CONCLUSIONS

In conclusion, on account of density functional theory calculations, we have systematically investigated the stability, magnetic, and electronic properties of the Ta_2O_3 monolayer with a honeycomb−Kagome lattice. The dynamical and thermal stabilities have been affirmed by molecular dynamics and phonon spectrum calculations. Furthermore, we confirm that this system is a room temperature ferromagnetic material and an

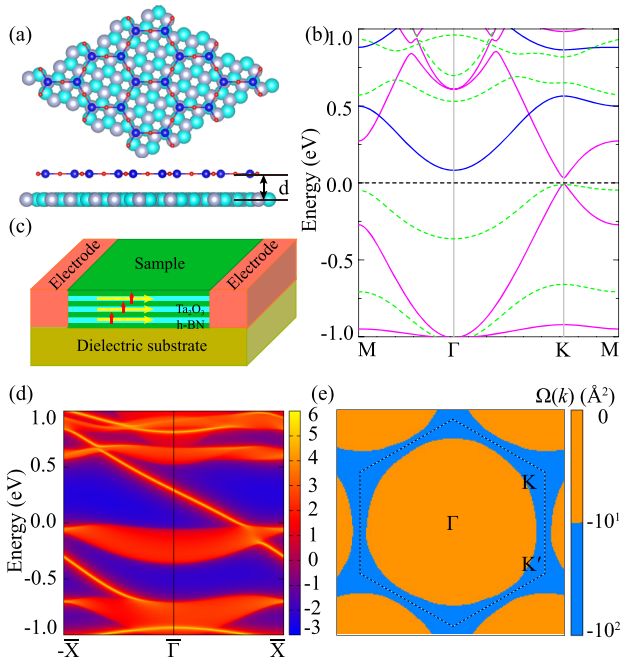

Figure 9. (a) Top and side views of the Ta_2O_3 monolayer on the h-BN substrate. (b) Band structure without and with SOC. The magenta and blue curves correspond to the spin-up and spin-down bands, respectively. Moreover, the band structure with SOC is plotted as a green dotted curve. (c) Schematic diagrams to realize the QAH effect in h-BN/Ta_2O_3/h-BN sandwiched heterostructures. The yellow and red arrows indicate the chiral edge currents and spin directions, respectively. (d) Calculated edge state of a semi-infinite sheet of Ta_2O_3/h-BN. (e) Calculated Berry curvature of Ta_2O_3/h-BN in the momentum space.

intrinsic QAH insulator with a Chern number of −1. More interestingly, the topological characteristic is robust when biaxial strain is applied with an enhanced band gap reaching up to 454.8 meV. Finally, we propose that the Ta_2O_3 monolayer could be synthesized on the h-BN substrate. Our findings provide an ideal platform for potential applications in low-power consumption spintronic devices.

ASSOCIATED CONTENT

Supporting Information

The Supporting Information is available free of charge at https://pubs.acs.org/doi/10.1021/acsaelm.1c00085.

Figures displaying the calculated band structures under various strains, band structures of the HSE06 method, details on the fitting of the TB wave function, and U value evaluated by linear response theory (PDF)

AUTHOR INFORMATION

Corresponding Authors

Yun Zhang − *Department of Physics and Information Technology, Baoji University of Arts and Sciences, Baoji 721016, People's Republic of China*; Email: zhangyun_xtu@163.com

Zhi-Xin Guo − *State Key Laboratory for Mechanical Behavior of Materials, Center for Spintronics and Quantum System, School of Materials Science and Engineering, Xi'an Jiaotong University, Xi'an, Shaanxi 710049, China*; Email: zxguo08@xjtu.edu.cn

https://doi.org/10.1021/acsaelm.1c00085
ACS Appl. Electron. Mater. 2021, 3, 1826−1833

Authors

Ping Li − *State Key Laboratory for Mechanical Behavior of Materials, Center for Spintronics and Quantum System, School of Materials Science and Engineering, Xi'an Jiaotong University, Xi'an, Shaanxi 710049, China;* orcid.org/0000-0001-8285-8921

Yue Ma − *Department of Physics and Information Technology, Baoji University of Arts and Sciences, Baoji 721016, People's Republic of China*

Complete contact information is available at: https://pubs.acs.org/10.1021/acsaelm.1c00085

Notes

The authors declare no competing financial interest.

■ ACKNOWLEDGMENTS

This work is supported by the National Natural Science Foundation of China (no. 12004295, no. 12074301, and no. 11704007) and the Science Fund for Distinguished Young Scholars of Hunan Province (no. 2018JJ1022). P.L. thanks China's Postdoctoral Science Foundation funded project (no. 2020M673364). Y.Z. thanks the Baoji University of Arts and Sciences Key Research (no. ZK16070). Z.-X.G. thanks the Fundamental Research Funds for Central Universities (no. xzy012019062).

■ REFERENCES

(1) Hasan, M. Z.; Kane, C. L. Colloquium: Topological insulators. *Rev. Mod. Phys.* **2010**, *82*, 3045.

(2) Nagaosa, N.; Sinova, J.; Onoda, S.; MacDonald, A. H.; Ong, N. P. Anomalous hall effect. *Rev. Mod. Phys.* **2010**, *82*, 1539.

(3) Qi, X.-L.; Zhang, S.-C. Topological insulators and superconductors. *Rev. Mod. Phys.* **2011**, *83*, 1057.

(4) Weng, H.; Yu, R.; Hu, X.; Dai, X.; Fang, Z. Quantum anomalous Hall effect and related topological electronic states. *Adv. Phys.* **2015**, *64*, 227.

(5) Haldane, F. D. M. Model for a Quantum Hall Effect without Landau Levels: Condensed-Matter Realization of the "Parity Anomaly". *Phys. Rev. Lett.* **1988**, *61*, 2015.

(6) Liu, C. X.; Qi, X. L.; Dai, X.; Fang, Z.; Zhang, S. C. Quantum Anomalous Hall Effect in Hg1-yMnyTe Quantum Wells. *Phys. Rev. Lett.* **2008**, *101*, 146802.

(7) Yu, R.; Zhang, W.; Zhang, H.-J.; Zhang, S.-C.; Dai, X.; Fang, Z. Quantized anomalous Hall effect in magnetic topological insulators. *Science* **2010**, *329*, 61.

(8) Qiao, Z.; Yang, S. A.; Feng, W.; Tse, W.-K.; Ding, J.; Yao, Y. G.; Wang, J.; Niu, Q. Quantum anomalous Hall effect in graphene from Rashba and exchange effects. *Phys. Rev. B: Condens. Matter Mater. Phys.* **2010**, *82*, 161414.

(9) Ding, J.; Qiao, Z.; Feng, W.; Yao, Y.; Niu, Q. Engineering quantum anomalous/valley Hall states in graphene via metal-atom adsorption: An ab-initio study. *Phys. Rev. B: Condens. Matter Mater. Phys.* **2011**, *84*, 195444.

(10) Qiao, Z.; Jiang, H.; Li, X.; Yao, Y.; Niu, Q. Microscopic theory of quantum anomalous Hall effect in graphene. *Phys. Rev. B: Condens. Matter Mater. Phys.* **2012**, *85*, 115439.

(11) Ezawa, M. Valley-polarized metals and quantum anomalous Hall effect in silicene. *Phys. Rev. Lett.* **2012**, *109*, 055502.

(12) Garrity, K. F.; Vanderbilt, D. Chern insulators from heavy atoms on magnetic substrates. *Phys. Rev. Lett.* **2013**, *110*, 116802.

(13) Wang, Z. F.; Liu, Z.; Liu, F. Quantum anomalous Hall effect in 2D organic topological insulators. *Phys. Rev. Lett.* **2013**, *110*, 196801.

(14) Qiao, Z.; Ren, W.; Chen, H.; Bellaiche, L.; Zhang, Z.; MacDonald, A. H.; Niu, Q. Quantum anomalous Hall effect in graphene proximity coupled to an antiferromagnetic insulator. *Phys. Rev. Lett.* **2014**, *112*, 116404.

(15) Liu, C.-C.; Zhou, J.-J.; Yao, Y. Valley-polarized quantum anomalous Hall phases and tunable topological phase transitions in half-hydrogenated Bi honeycomb monolayers. *Phys. Rev. B: Condens. Matter Mater. Phys.* **2015**, *91*, 165430.

(16) Li, P.; Li, X.; Zhao, W.; Chen, H.; Chen, M.-X.; Guo, Z.-X.; Feng, J.; Gong, X.-G.; MacDonald, A. H. Topological Dirac States beyond π-Orbitals for Silicene on SiC(0001) Surface. *Nano Lett.* **2017**, *17*, 6195.

(17) Wang, H. P.; Luo, W.; Xiang, H. J. Prediction of high-temperature quantum anomalous Hall effect in two-dimensional transition-metal oxides. *Phys. Rev. B* **2017**, *95*, 125430.

(18) Sun, Q.; Kioussis, N. Prediction of manganese trihalides as two-dimensional Dirac half-metals. *Phys. Rev. B* **2018**, *97*, 094408.

(19) Li, P. Prediction of intrinsic two dimensional ferromagnetism realized quantum anomalous Hall effect. *Phys. Chem. Chem. Phys.* **2019**, *21*, 6712.

(20) Wang, K.; Zhang, Y.; Zhao, W.; Li, P.; Ding, J.-W.; Xie, G.-F.; Guo, Z.-X. Topological Dirac states in transition-metal monolayers on graphyne. *Phys. Chem. Chem. Phys.* **2019**, *21*, 9310.

(21) Li, P. Stanene on a SiC(0001) surface: a candidate for realizing quantum anomalous Hall effect. *Phys. Chem. Chem. Phys.* **2019**, *21*, 11150.

(22) Li, P.; Cai, T.-Y. Fully spin-polarized quadratic non-Dirac bands realized quantum anomalous Hall effect. *Phys. Chem. Chem. Phys.* **2020**, *22*, 549.

(23) Li, P.; Cai, T.-Y. Two-Dimensional Transition-Metal Oxides Mn2O3 Realized the Quantum Anomalous Hall Effect. *J. Phys. Chem. C* **2020**, *124*, 12705.

(24) Chang, C.-Z.; Zhang, J.; Feng, X.; Shen, J.; Zhang, Z.; Guo, M.; Li, K.; Ou, Y.; Wei, P.; Wang, L.-L.; Ji, Z.-Q.; Feng, Y.; Ji, S.; Chen, X.; Jia, J.; Dai, X.; Fang, Z.; Zhang, S.-C.; He, K.; Wang, Y.; Lu, L.; Ma, X.-C.; Xue, Q.-K. Experimental Observation of the Quantum Anomalous Hall Effect in a Magnetic Topological Insulator. *Scienece* **2013**, *340*, 167.

(25) Kou, X.; Gou, S.-T.; Fan, Y.; Pan, L.; Lang, M.; Jiang, Y.; Shao, Q.; Nie, T.; Murata, K.; Tang, J.; Wang, Y.; He, L.; Lee, T.-K.; Lee, W.-L.; Wang, K.-L. Scale-invariant quantum anomalous Hall effect in magnetic topological insulators beyond the two-dimensional limit. *Phys. Rev. Lett.* **2014**, *113*, 137201.

(26) Chang, C.-Z.; Zhao, W.; Kim, D. Y.; Zhang, H.; Assaf, B. A.; Heiman, D.; Zhang, S.-C.; Liu, C.; Chan, M. H. W.; Moodera, J. S. High-precision realization of robust quantum anomalous Hall state in a hard ferromagnetic topological insulator. *Nat. Mater.* **2015**, *14*, 473.

(27) Deng, Y.; Yu, Y.; Shi, M. Z.; Guo, Z.; Xu, Z.; Wang, J.; Chen, X. H.; Zhang, Y. Quantum anomalous Hall effect in intrinsic magnetic topological insulator MnBi2Te4. *Science* **2020**, *367*, 895.

(28) Kresse, G.; Hafner, J. Ab initiomolecular dynamics for liquid metals. *Phys. Rev. B: Condens. Matter Mater. Phys.* **1993**, *47*, 558.

(29) Kresse, G.; Joubert, D. From ultrasoft pseudopotentials to the projector augmented-wave method. *Phys. Rev. B: Condens. Matter Mater. Phys.* **1999**, *59*, 1758.

(30) Perdew, J. P.; Burke, K.; Ernzerhof, M. Generalized Gradient Approximation Made Simple. *Phys. Rev. Lett.* **1996**, *77*, 3865.

(31) Togo, A.; Oba, F.; Tanaka, I. First-principles calculations of the ferroelastic transition between rutile-type and CaCl2-type SiO2 at high pressures. *Phys. Rev. B: Condens. Matter Mater. Phys.* **2008**, *78*, 134106.

(32) Dudarev, S. L.; Botton, G. A.; Savrasov, S. Y.; Humphreys, C. J.; Sutton, A. P. Electron-energy-loss spectra and the structural stability of nickel oxide: An LSDA+U study. *Phys. Rev. B: Condens. Matter Mater. Phys.* **1998**, *57*, 1505.

(33) Cococcioni, M.; Gironcoli, S. De. Linear response approach to the calculation of the effective interaction parameters in the LDA+U method. *Phys. Rev. B: Condens. Matter Mater. Phys.* **2005**, *71*, 035105.

(34) Marzari, N.; Vanderbilt, D. Maximally localized generalized Wannier functions for composite energy bands. *Phys. Rev. B: Condens. Matter Mater. Phys.* **1997**, *56*, 12847.

(35) Mostofi, A. A.; Yates, J. R.; Lee, Y.-S.; Souza, I.; Vanderbilt, D.; Marzari, N. wannier90: A tool for obtaining maximally-localised Wannier functions. *Comput. Phys. Commun.* **2008**, *178*, 685.

(36) Sancho, M. P. L.; Sancho, J. M. L.; Rubio, J. Quick iterative scheme for the calculation of transfer matrices: application to Mo (100). *J. Phys. F: Met. Phys.* **1984**, *14*, 1205.
(37) Wu, Q.; Zhang, S.; Song, H.-F.; Troyer, M.; Soluyanov, A. A. WannierTools: An open-source software package for novel topological materials. *Comput. Phys. Commun.* **2018**, *224*, 405.
(38) Lu, J.-L.; Luo, W.; Li, X.-Y.; Yang, S.-Q.; Cao, J.-X.; Gong, X.-G.; Xiang, H.-J. Two-Dimensional Node-Line Semimetals in a Honeycomb-Kagome Lattice *. *Chin. Phys. Lett.* **2017**, *34*, 057302.
(39) Ji, W.-x.; Zhang, B.-m.; Zhang, S.-f.; Zhang, C.-w.; Ding, M.; Li, P.; Wang, P.-j. A planar C3Ca2 film: a novel 2p Dirac half metal. *J. Mater. Chem. C* **2017**, *5*, 8504.
(40) Liu, Z.; Wang, Z.-F.; Mei, J.-W.; Wu, Y.-S.; Liu, F. Flat Chern Band in a Two-Dimensional Organometallic Framework. *Phys. Rev. Lett.* **2013**, *110*, 106804.
(41) Wang, Z. F.; Su, N.; Liu, F. Prediction of a Two-Dimensional Organic Topological Insulator. *Nano Lett.* **2013**, *13*, 2842.
(42) Kambe, T.; Sakamoto, R.; Hoshiko, K.; Takada, K.; Miyachi, M.; Ryu, J.-H.; Sasaki, S.; Kim, J.; Nakazato, K.; Takata, M.; Nishihara, H. π-Conjugated Nickel Bis(dithiolene) Complex Nanosheet. *J. Am. Chem. Soc.* **2013**, *135*, 2462.
(43) Zhang, X.; Wang, Z.; Zhao, M.; Liu, F. Tunable topological states in electron-doped HTT-Pt. *Phys. Rev. B* **2016**, *93*, 165401.
(44) Wang, A.; Zhao, X.; Zhao, M.; Zhang, X.; Feng, Y.; Liu, F. Kane Fermion in a Two-Dimensional π-Conjugated Bis(iminothiolato)-nickel Monolayer. *J. Phys. Chem. Lett.* **2018**, *9*, 614.
(45) Henkelman, G.; Arnaldsson, A.; Jónsson, H. A fast and robust algorithm for Bader decomposition of charge density. *Comput. Mater. Sci.* **2006**, *36*, 354.
(46) Xiang, H. J.; Wei, S.-H.; Whangbo, M.-H. Origin of the Structural and Magnetic Anomalies of the Layered Compound SrFeO2: A Density Functional Investigation. *Phys. Rev. Lett.* **2008**, *100*, 167207.
(47) Liu, C.-X.; Zhang, S.-C.; Qi, X.-L. The Quantum Anomalous Hall Effect: Theory and Experiment. *Annu. Rev. Condens. Matter Phys.* **2016**, *7*, 301.
(48) Liu, C.-C.; Feng, W.; Yao, Y. Quantum Spin Hall Effect in Silicene and Two-Dimensional Germanium. *Phys. Rev. Lett.* **2011**, *107*, 076802.
(49) Xu, Y.; Yan, B.; Zhang, H.-J.; Wang, J.; Xu, G.; Tang, P.; Duan, W.; Zhang, S.-C. Large-gap quantum spin Hall insulators in tin films. *Phys. Rev. Lett.* **2013**, *111*, 136804.
(50) Li, P.; Cao, J.; Guo, Z.-X. A new approach for fabricating germanene with Dirac electrons preserved: a first principles study. *J. Mater. Chem. C* **2016**, *4*, 1736.
(51) Zhang, L.; Zhang, S.-f.; Ji, W.-x.; Zhang, C.-w.; Li, P.; Wang, P.-j.; Li, S.-s.; Yan, S.-s. Discovery of a novel spin-polarized nodal ring in a two-dimensional HK lattice. *Nanoscale* **2018**, *10*, 20748.
(52) Sancho, M. P. L.; Sancho, J. M. L.; Sancho, J. M. L.; Rubio, J. Highly convergent schemes for the calculation of bulk and surface Green functions. *J. Phys. F: Met. Phys.* **1985**, *15*, 851.
(53) Souza, I.; Marzari, N.; Vanderbilt, D. Maximally localized Wannier functions for entangled energy bands. *Phys. Rev. B: Condens. Matter Mater. Phys.* **2001**, *65*, 035109.
(54) Wang, X.; Yates, J. R.; Souza, I.; Vanderbilt, D. Ab initio calculation of the anomalous Hall conductivity by Wannier interpolation. *Phys. Rev. B: Condens. Matter Mater. Phys.* **2006**, *74*, 195118.
(55) Addou, R.; Dahal, A.; Batzill, M. Growth of a two-dimensional dielectric monolayer on quasi-freestanding graphene. *Nat. Nanotechnol.* **2013**, *8*, 41.

https://doi.org/10.1021/acsaelm.1c00085
ACS Appl. Electron. Mater. 2021, 3, 1826−1833